Check for updates

Giant second-harmonic generation in ferroelectric NbOI$_2$

Ibrahim Abdelwahab [1,2], Benjamin Tilmann [2], Yaze Wu [3,4], David Giovanni[5], Ivan Verzhbitskiy [3,4], Menglong Zhu[1], Rodrigo Berté [2,6], Fengyuan Xuan [4], Leonardo de S. Menezes [2,7], Goki Eda [3,4], Tze Chien Sum [5], Su Ying Quek[3,4,8,9], Stefan A. Maier [2,10,11 ✉] and Kian Ping Loh [1,4 ✉]

Implementing nonlinear optical components in nanoscale photonic devices is challenged by phase-matching conditions requiring thicknesses in the order of hundreds of wavelengths, and is disadvantaged by the short optical interaction depth of nanometre-scale materials and weak photon–photon interactions. Here we report that ferroelectric NbOI$_2$ nanosheets exhibit giant second-harmonic generation with conversion efficiencies that are orders of magnitude higher than commonly reported nonlinear crystals. The nonlinear response scales with layer thickness and is strain- and electrical-tunable; a record >0.2% absolute SHG conversion efficiency and an effective nonlinear susceptibility $\chi_{eff}^{(2)}$ in the order of 10^{-9} m V^{-1} are demonstrated at an average pump intensity of 8 kW cm^{-2}. Due to the interplay between anisotropic polarization and excitonic resonance in NbOI$_2$, the spatial profile of the polarized SHG response can be tuned by the excitation wavelength. Our results represent a new paradigm for ultrathin, efficient nonlinear optical components.

Materials lacking inversion symmetry have a non-vanishing second-order nonlinear optical susceptibility. When this is combined with a permanent polarization, they can exhibit strong second-harmonic generation (SHG)[1]. SHG refers to the frequency doubling of a light wave and it is of paramount importance for applications such as coherent light generation, nonlinear auto- and cross-correlations, optical signal processing and imaging[2–7]. Furthermore, SHG is an optimal tool to probe material properties such as crystal symmetry, relative orientation, polar domains, magnetic ordering, surfaces and quantum interference[8–13]. However, the inherently weak photon–photon interactions in classical inversion-asymmetric materials demand high-intensity pumping, bulky interaction volumes, and complex phase-matching techniques to achieve appreciable SHG responses. This prevents the realization of miniature nonlinear optical devices that can function at moderate input powers.

Two-dimensional ferroelectric materials (materials possessing a spontaneous electric polarization, P_s) are a relatively new class of ultrathin materials, with potential applications in memory devices[14]. Ferroelectricity breaks the material's inversion symmetry, thus two-dimensional ferroelectrics are excellent candidates for realizing strong nonlinear responses over nanometre-scale interaction lengths. Layered niobium oxide dihalides NbOX$_2$ (X = Cl, Br, I)[15–18] have a Peierls-distorted polar structure due to their anisotropic bonding along the in-plane b and c directions: only the b direction is polar, giving rise to strongly anisotropic ferroelectricity. Our density functional perturbation theory calculations predicted very large in-plane ferroelectric and piezoelectric responses for the NbOX$_2$ family ($P_s = 1.43 \times 10^{-10}$ C m^{-1} and piezoelectric stress tensor

element $e_{22} = 31.6 \times 10^{-10}$ C m^{-1} for NbOI$_2$ monolayer)[19]. Given that the SHG intensity is proportional to spontaneous polarization[20], NbOX$_2$ is therefore highly promising for exploring large second-order optical nonlinearities.

Here we report that 20-nm-thick NbOI$_2$ flakes exhibit ultra-strong, electrically tunable SHG with an absolute conversion efficiency of 0.006%, which is orders of magnitude larger than values reported for other two-dimensional materials[21–26], Weyl semi-metals[27] and conventional nonlinear materials[28–31]. Straining (~3%) the crystal along the polar direction leads to a 35-fold enhancement of the SHG efficiency, achieving an effective SHG susceptibility $\chi_{eff}^{(2)}$ of 113×10^{-11} m V^{-1} and absolute conversion efficiency of >0.2%. The SHG response can be switched from highly anisotropic to isotropic by tuning the wavelength around the exciton resonance.

Results

Structure characterization. Centimetre-sized NbOI$_2$ single crystals were grown by chemical vapour transport (CVT) (see the Methods for more details). The crystal structure of NbOI$_2$ was resolved using single-crystal X-ray diffraction (SC-XRD) measurements. Bulk NbOI$_2$ crystallizes in a monoclinic crystal structure with space group $C2$ (Supplementary Table 1 and Supplementary Crystallographic Information Files (CIFs) contain the crystallographic data). Each NbOI$_2$ layer is composed of NbO$_2$I$_4$ octahedra, which link together by sharing the opposite iodine corners along the crystallographic c-axis and by sharing the opposite oxygen corners along the b-axis, as shown in Fig. 1a. A first-order Peierls distortion occurs along the c-axis[32], which leads to the dimerization

[1]Department of Chemistry, National University of Singapore, Singapore, Singapore. [2]Chair in Hybrid Nanosystems, Nanoinstitute Munich, Faculty of Physics, Ludwig-Maximilians-Universität München, Munich, Germany. [3]Department of Physics, National University of Singapore, Singapore, Singapore. [4]Centre for Advanced 2D Materials and Graphene Research Centre, National University of Singapore, Singapore, Singapore. [5]School of Physical and Mathematical Sciences, Nanyang Technological University, Singapore, Singapore. [6]Instituto de Física, Universidade Federal de Goiás, Goiania, Brazil. [7]Departamento de Física, Universidade Federal de Pernambuco, Recife, Brazil. [8]NUS Graduate School, Integrative Sciences and Engineering Programme, National University of Singapore, Singapore, Singapore. [9]Department of Materials Science and Engineering, National University of Singapore, Singapore, Singapore. [10]School of Physics and Astronomy, Monash University, Melbourne, Victoria, Australia. [11]Department of Physics, Imperial College London, London, UK. ✉e-mail: Stefan.Maier@monash.edu; chmlohkp@nus.edu.sg
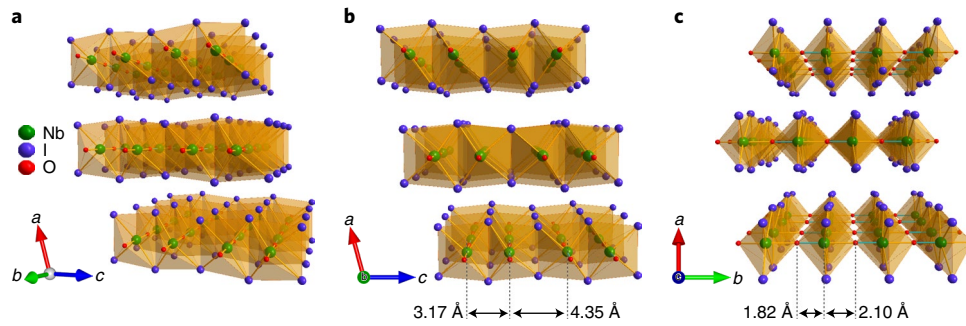
Fig. 1 | Atomic structure of ferroelectric layered $NbOI_2$. a, Three-dimensional schematic diagram of trilayer $NbOI_2$ monoclinic crystal structure (space group $C2$). Each $NbOI_2$ layer is composed of NbO_2I_4 octahedra linked together by sharing the opposite iodine corners along the crystallographic c-axis and by sharing the opposite oxygen corners along the b-axis. **b**, A side view of trilayer $NbOI_2$ along the non-polar c-axis showing an alternation of short and long Nb–Nb distances. **c**, A side view of trilayer $NbOI_2$ along the polar b-axis showing an alternation of two unequal Nb–O bond lengths. The Nb–Nb···Nb alternation is 3.17 and 4.35 Å, whereas the Nb–O···Nb alternation is 1.82 and 2.10 Å along the c- and b-axes, respectively. The thickness of $NbOI_2$ monolayer is 0.73 nm.

of niobium atoms. Consequently, an alternation of short and long Nb–Nb bond distances occurs along the NbI_4 chain direction (Fig. 1b). Furthermore, there occurs a second-order Peierls distortion along the b-axis, through which the niobium ions are displaced from the centre positions of the octahedra towards one of the bridging oxygen atoms. As a result, an alternation of two unequal Nb–O bond lengths takes place (Fig. 1c), giving rise to spontaneous polarization. The Peierls distortions are energetically favourable as they lower the total electronic energy of the $NbOI_2$ system (Supplementary Note 1). The Nb–Nb···Nb alternation is 3.17 and 4.35 Å, whereas the Nb–O···Nb alternation is 1.82 and 2.10 Å along the c- and b-axes, respectively. The large niobium off-centre polar displacement (~0.14 Å) along the b-axis drives a robust in-plane ferroelectric polarization, which is among the highest P_s values in the two-dimensional ferroelectrics family[19,33].

Anisotropic band structure. The anisotropic band structure of $NbOI_2$ is responsible for its large anisotropic optical properties. Figure 2a displays the density functional theory (DFT)-calculated energy-band structure of $NbOI_2$ monolayer with projection on atomic orbitals. The polar (Nb–O···Nb) and non-polar (Nb–Nb···Nb) directions correspond with the $\Gamma \rightarrow Y$ and $\Gamma \rightarrow X$ directions in the reciprocal space (k-space), respectively. The bottom four conduction bands are denoted as c_1, c_2, c_3 and c_4, and arise primarily from niobium d orbitals. The top four valence bands are denoted as v_1, v_2, v_3 and v_4. Although most of the valence bands are attributed to iodine p orbitals, the highest energy valence band v_1 arises from niobium $d_{x^2-y^2}$ and d_{z^2} orbitals due to the splitting of the niobium $d_{x^2-y^2}/d_{z^2}$ bands resulting from Peierls distortion (Supplementary Note 1). Strikingly, there is strong mixing between the $d_{x^2-y^2}$ and d_{z^2} orbitals in v_1 and c_3 throughout the entire Brillouin zone. The material has fully occupied valence bands and the nearly flat v_1 band implies that the v_1 electrons are highly localized. The GW [34,35]-calculated band structure of $NbOI_2$ (Supplementary Fig. 1) indicates that the valence band maximum occurs at Y, while the conduction band minimum occurs at X (within the c_2 band), giving an indirect bandgap ($E_g = 2.24$ eV).

The band structure is more dispersive along the polar direction than the non-polar direction. As k varies from Γ to Y, the magnitude of the π-bond overlap between the niobium d_{yz} (d_{xy}) and oxygen p_z (p_x) orbitals increases quite substantially, bringing about highly dispersive c_1 and c_2 bands. The c_1 and c_2 bands are nevertheless weakly dispersive on going from Γ to X. This is due to the opposing effects of the metal–metal (Nb (d_{yz})–Nb (d_{yz})) and metal–ligand (Nb (d_{yz})–I (p_y)) π-bond interactions at X as well as the weak Nb (d_{xy})–Nb

(d_{xy}) δ-bond interaction[36]. Similarly, the v_2 band varies rapidly in energy from Γ to Y and smoothly from Γ to X. We have carried out angle-resolved photoemission spectroscopy (ARPES) measurements to confirm the band structure of $NbOI_2$. The valence-band ARPES spectra of $NbOI_2$ clearly show the dispersive feature of the v_2 band along Γ–Y, and the dispersionless feature of the bands along Γ–X (Fig. 2b), in good agreement with the band-structure calculations. A comparison of the ARPES results with the GW band structure shows good quantitative agreement; the similar valence band structure between monolayer (theory) and bulk (experiment) $NbOI_2$ indicates that the band dispersion does not vary with thickness, which is different from transition metal dichalcogenides (TMDs) and graphene. Interlayer interactions in bulk $NbOI_2$ induce band splitting for the bands that arise from out-of-plane orbitals (Supplementary Fig. 2). This can explain the broadening observed for some bands in the ARPES band structure.

Linear optical response. In line with its anisotropic band structure, the linear optical properties of $NbOI_2$ are markedly different along the polar and non-polar directions, which is confirmed by performing Mueller matrix ellipsometry measurements over a wide spectral range (6.2–0.65 eV, 200–1,900 nm). The extracted imaginary part of the dielectric function (ε_2) is shown in Fig. 2c. We observe two predominant peaks confined along the non-polar direction in the visible range (at $P_1 = 2.34$ eV, 530 nm; and $P_2 = 2.64$ eV, 470 nm) and one broad peak confined along the polar direction in the near ultraviolet range (at $P_4 = 3.54$ eV, 350 nm). According to our GW-BSE calculations, peaks P_1 to P_4 are excitonic in nature. The presence of strong optical anisotropy is also reflected from polarization-dependent absorption and transmission measurements (Supplementary Figs. 3 and 4, and Supplementary Video 1). In line with the ellipsometry data, two absorption peaks at ~530 nm and 470 nm are detected when light is linearly polarized along the non-polar direction of $NbOI_2$ (Supplementary Fig. 3). By contrast, a much weaker absorption in the visible range is collected when light is polarized along the polar direction. Moreover, no circular dichroism signal was observed under circular optical excitation (Supplementary Fig. 5), excluding any optical activity (chirality) in $NbOI_2$.

Nonlinear optical response. We isolate $NbOI_2$ flakes of sub-100-nm thicknesses from a single crystal for nonlinear optical study. The $NbOI_2$ nanosheets were encapsulated with a thin layer of transparent hexagonal boron nitride (h-BN) to avoid any photo-oxidation effects. There are eight non-vanishing SHG tensor elements for space group C2: d_{14}, d_{16}, d_{21}, d_{22}, d_{23}, d_{25}, d_{34} and
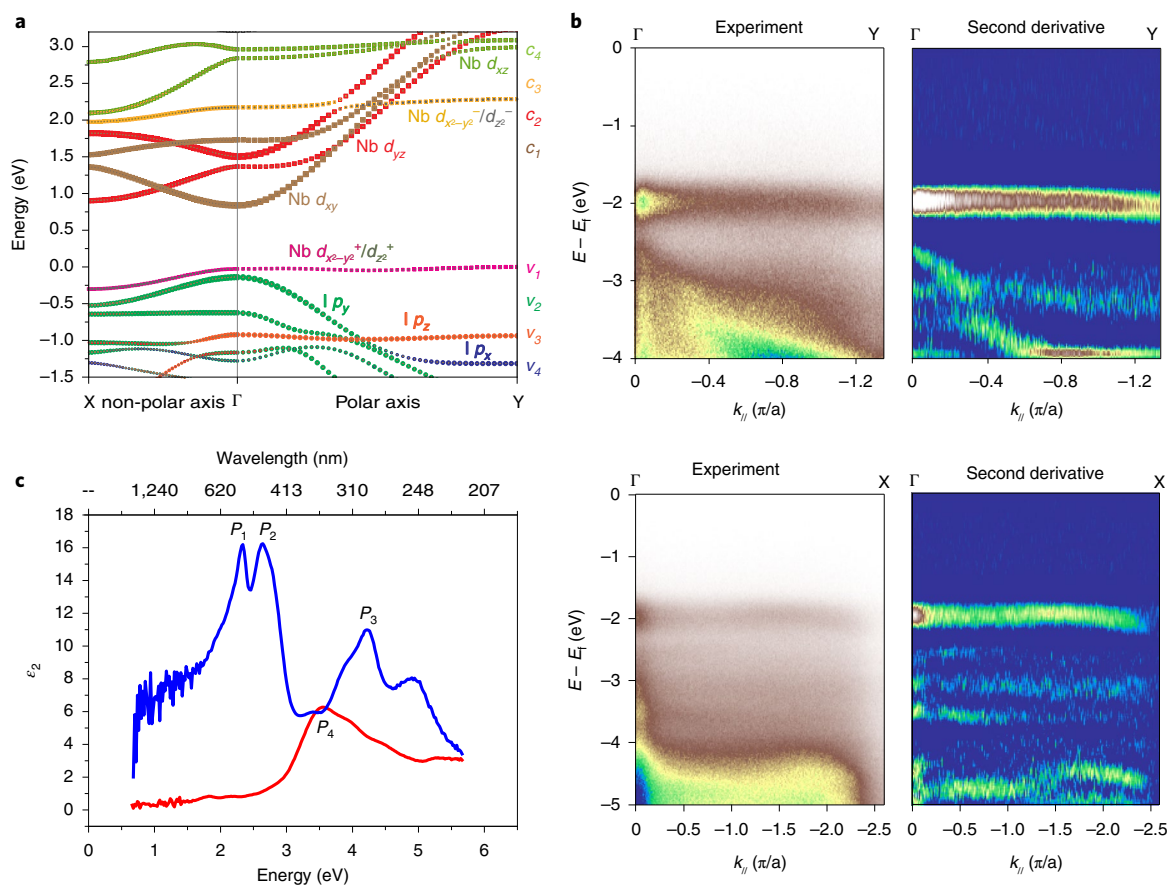
Fig. 2 | Anisotropic band structure and linear optical response of NbOI$_2$. a, Density functional theory-calculated band structure of NbOI$_2$ monolayer. The $\Gamma \rightarrow$ Y and $\Gamma \rightarrow$ X high-symmetry directions in the reciprocal space (k-space) correspond respectively to the polar (Nb–O···Nb) and non-polar (Nb–Nb···Nb) directions of NbOI$_2$ in real space, respectively. The valence band maximum is set to zero. Orbital component analysis is elucidated by different colours: v_1 (magenta/grey, niobium orbital $d_{x^2-y^2+}/d_{z^2+}$), v_2 (green, iodine orbital p_y), v_3 (orange, iodine orbital p_z), v_4 (blue, iodine orbital p_x); c_1 (brown, niobium orbital d_{xy}), c_2 (red, niobium orbital d_{yz}), c_3 (yellow/grey, niobium orbital $d_{x^2-y^2-}/d_{z^2-}$), c_4 (olive, niobium orbital d_{xz}). The + and – superscripts for the niobium $d_{x^2-y^2}$ and niobium d_{z^2} orbitals refer to the energy-split v_1 (+) and c_3 (–) $d_{x^2-y^2}/d_{z^2}$ bands due to Peierls distortion. The x, y, z directions correspond to the a, b, c crystal axes of the NbOI$_2$ unit cell, respectively. **b**, ARPES intensity plots and their corresponding second-derivative plots of NbOI$_2$ along the polar (top) and non-polar (bottom) directions, where $k_{//}$ is the in-plane component of electron momentum. The Fermi level is at zero. **c**, The imaginary dielectric function ε_2 of NbOI$_2$ along the polar (red) and non-polar (blue) directions, obtained by Mueller matrix ellipsometry measurements. Our GW-BSE calculations reveal that the P_1 and P_2 excitons arise from transitions from v_1, v_2 and v_3 to c_1.

d_{36} (Supplementary Note 2), where the SHG susceptibility $\chi_{ijk}^{(2)}$ can be calculated by $\chi_{ijk}^{(2)} = 2d_{ij}$. Considering the Kleinman symmetry, $d_{16} = d_{21}$; $d_{14} = d_{25} = d_{36}$; and $d_{23} = d_{34}$; the spontaneous polarization in NbOI$_2$ induces an extremely large d_{22} coefficient (that is, the SHG tensor element along the polar axis). To selectively probe the d_{22} coefficient, we pumped NbOI$_2$ nanosheets supported on a quartz substrate (Fig. 3a) with normally incident (along the a-axis) femtosecond laser pulses whose linear polarization is parallel to the polar direction of NbOI$_2$. Figure 3b shows resultant SHG intensity maps of the sample at two representative SHG wavelengths ($\lambda_{SHG} = 450$ and 500 nm). Notably, a highly efficient SHG signal covering $\lambda_{SHG} = 425–525$ nm is detected for the NbOI$_2$ flakes (Fig. 3b and Supplementary Fig. 6), with negligible background contribution from the quartz substrate. The strong broadband d_{22}-SHG emission attained at low optical pumping losses (refer to the red curve in Fig. 2c) is a direct consequence of the large ferroelectricity of NbOI$_2$. When the excitation wavelength is detuned below $\lambda_{pump} = 800$ nm, we find that the SHG emission intensity is reduced significantly, and the two-photon absorption (2PA) process emerges (Supplementary Fig. 7). This is anticipated, as the excitation photon energy is high enough $\left(\hbar\omega > \frac{1}{2}E_g\right)$ to allow two-photon absorption to populate the

conduction band of NbOI$_2$ and, as a result, the slow band-to-band two-photon absorption nonlinearity greatly outweighs the instantaneous SHG nonlinearity[1].

In accordance with the second-order nature of the process, the generated SHG power in NbOI$_2$ maintains a quadratic dependence on the average input laser power up to ~80 µW (2.2 kW peak power, $\lambda_{pump} = 1{,}050$ nm), as shown in Fig. 3c for 20-nm-thick NbOI$_2$. Neither saturation nor hysteresis behaviour in the SHG profile was observed up to the maximum input power used, ruling out any laser-induced material damage. In addition to their thermal stability under laser illumination, the optical properties of NbOI$_2$ flakes show remarkable air stability over several months (Supplementary Fig. 8). Remarkably, an absolute SHG conversion efficiency (η_{SHG})—calculated as the ratio between SHG and excitation powers ($\eta_{SHG} = P_{SHG}/P_{pump}$)—of ~0.006% is attained for the NbOI$_2$ nanoflakes at $\lambda_{pump} = 1{,}050$ nm (η_{SHG} is on the order of 0.0001% for NbOI$_2$ monolayer), which is orders of magnitude higher than the values previously reported for other nonlinear two-dimensional materials (Supplementary Table 2). The measured SHG efficiency (0.006%) at 1,000–1,050 nm excitation is also orders of magnitude higher than that reported for NbOI$_2$ flake of similar thickness excited
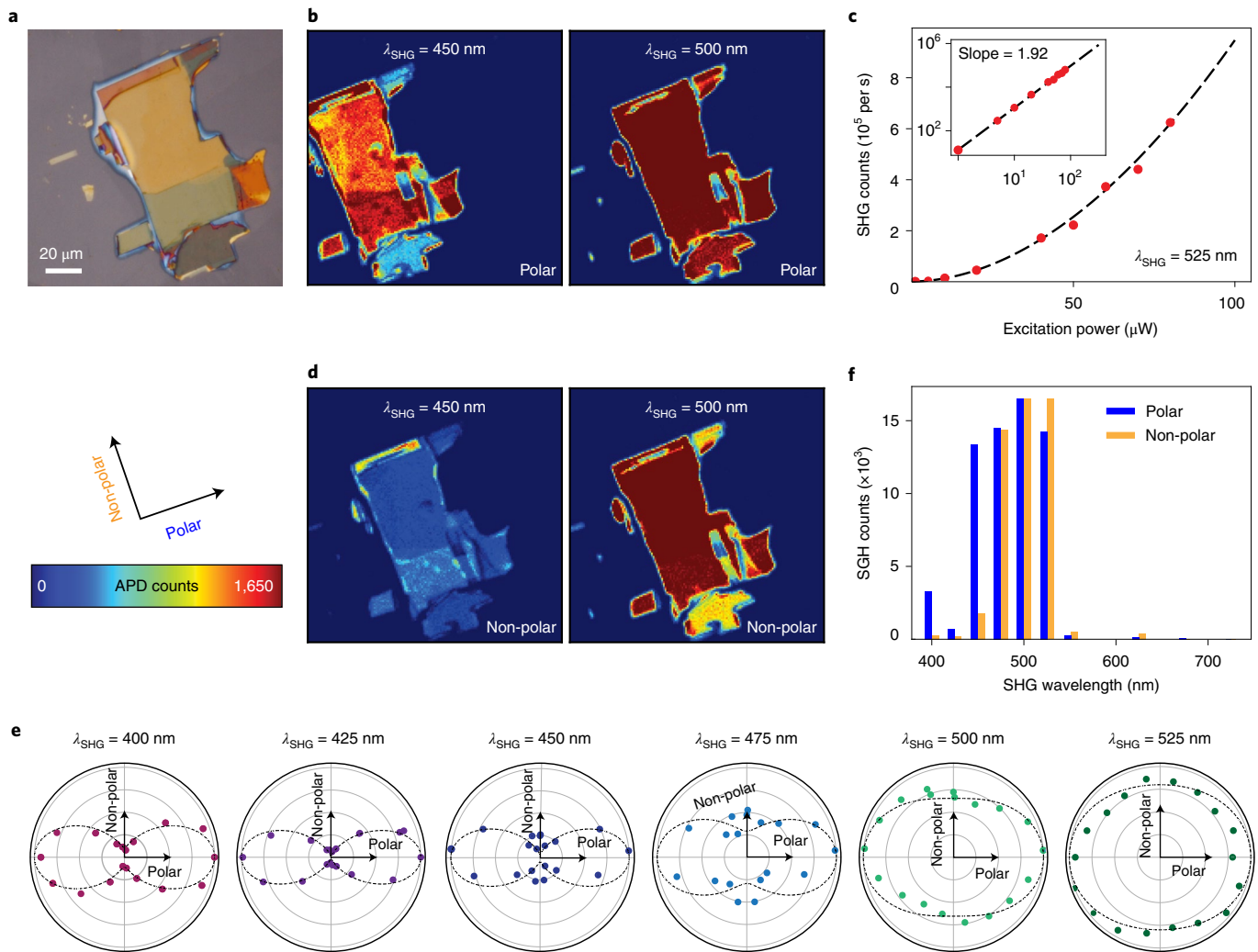
Fig. 3 | Characterization of SHG in NbOI₂. a, Optical image of NbOI₂ flake on quartz substrate after encapsulation with *h*-BN. **b**, SHG intensity maps recorded with an avalanche photodiode (APD) of the sample shown in **a** at $\lambda_{SHG} = 450\,nm$ and 500 nm, obtained by setting the excitation polarization parallel to the polar direction of NbOI₂. **c**, Excitation power dependence of the SHG signal (red dots) with quadratic fit (dash curve) at $\lambda_{SHG} = 525\,nm$ for 20-nm-thick NbOI₂ flake. The inset shows the linear fit of the log–log plot with a slope equal to 1.92. **d**, SHG intensity maps of the sample in **a** at $\lambda_{SHG} = 450\,nm$ and 500 nm obtained by setting the excitation polarization parallel to the non-polar direction of NbOI₂. All the maps in **b** and **d** are acquired using equally intense excitation pulses. **e**, Polar plots of the total SHG intensity as a function of the polarization angle of the excitation beam at $\lambda_{SHG} = 400$–525 nm. The coloured dots represent the experimental data while the dash lobes represent the theoretical (considering the Kleinman symmetry) predictions of the SHG intensity as a function of the input polarization. **f**, Bar chart showing the polar and non-polar SHG signals from the NbOI₂ flake in the range of $\lambda_{SHG} = 400$–750 nm while maintaining constant excitation intensities. The polar SHG signal is 7.6-times the non-polar signal at 450 nm, but their signals reach similar intensities between 475 to 525 nm.

by a 1,200 nm pump in ref. [37] ($191 \times \eta_{MoS_2} \approx 10^{-6}\%$). As shown in Supplementary Fig. 6, the SHG response substantially drops for input wavelengths above 1050 nm.

The effective bulk-like SHG susceptibility $\chi_{eff}^{(2)}$ of NbOI₂ can be obtained by dividing the SHG sheet susceptibility $\chi_s^{(2)}$ (as calculated in ref. [22]) by the NbOI₂ flake thickness. We estimate an $\chi_{eff}^{(2)}$ of ~19 $\times 10^{-11}\,m\,V^{-1}$, which is larger than those of commonly used non-linear crystals (for example, LiNbO₃ with $5.2 \times 10^{-11}\,m\,V^{-1}$). This is corroborated by the large d_{22}-SHG coefficients that we have calculated within the independent particle approximation using DFT (Supplementary Note 3 and Supplementary Fig. 9). The calculations predict large d_{22}-SHG coefficients corresponding to outgoing photon energies in the range ~2.0–2.6 eV (peaks B and C), as well as ~1.3–1.5 eV (peak A). The interband transitions giving rise to these peaks are shown in Supplementary Table 3. We expect that electron

self-energy effects will blue shift these peaks, while excitonic effects may increase the maximum SHG amplitudes.

The AB Bernal stacking of many two-dimensional materials (for example, the 2H phases of group-VI TMDs) results in ultrathin flakes with thickness corresponding to even-layer number unit cells to be inversion symmetric and SHG-inactive, and only ultrathin flakes with thickness corresponding to odd-layer number unit cells can be SHG-active. This effectively constrains the nonlinear response to atomically thin interaction lengths for many TMD materials that possess bulk inversion symmetry. By contrast, NbOI₂ has a broken inversion symmetry regardless of thickness and its SHG response scales with thickness. Taking into consideration the coherence length of the generated SHG radiation and interference effects[38,39], the $\chi_s^{(2)}$ of AA-stacked NbOI₂ scales with thickness (Supplementary Fig. 10), rendering NbOI₂ practically useful for
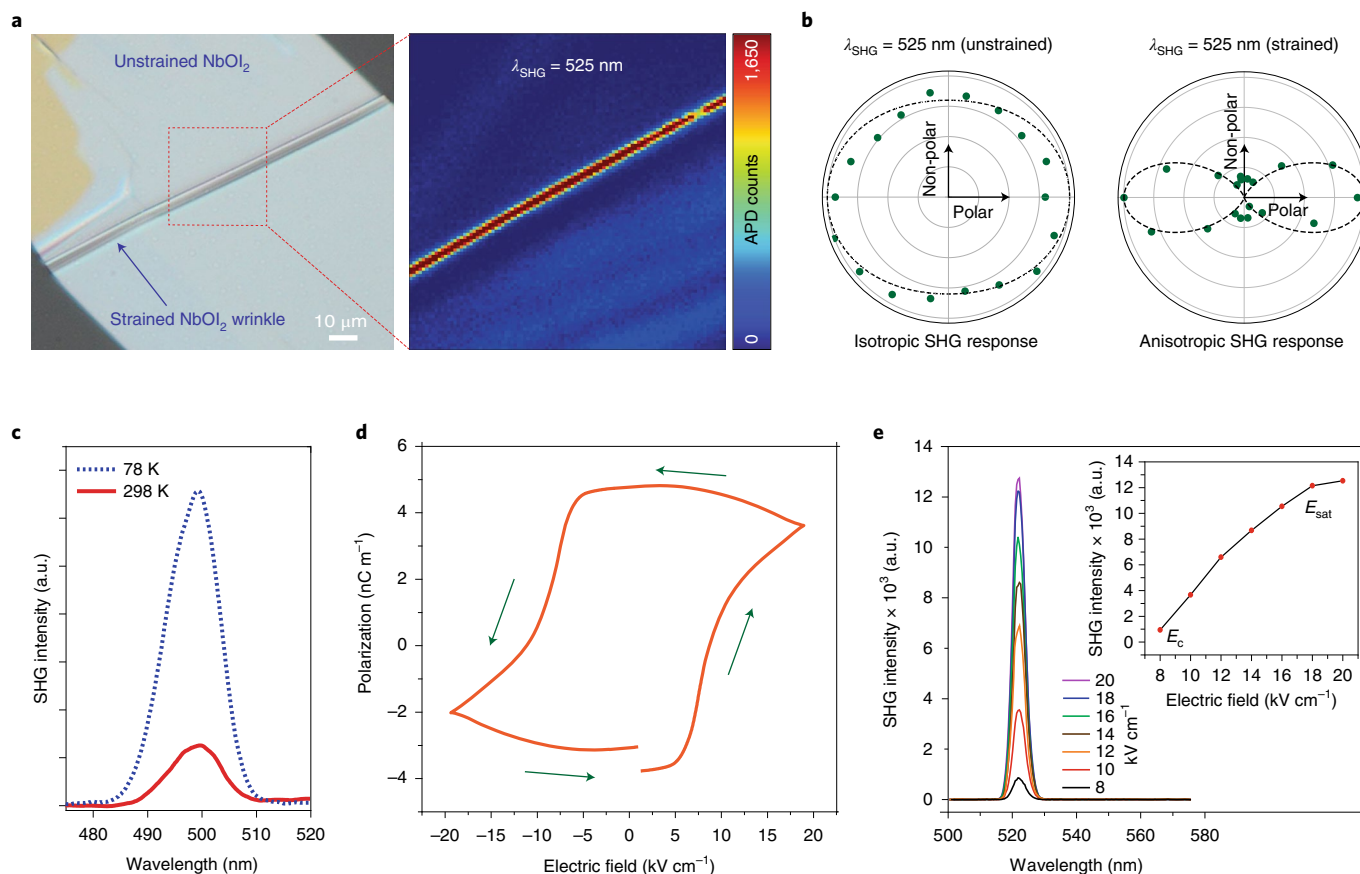
Fig. 4 | Effects of strain, temperature and electric fields on SHG in NbOI$_2$. a, Optical image of a wrinkled NbOI$_2$ flake (left), and corresponding SHG map at $\lambda_{SHG} = 525$ nm (right). **b**, Polar plots of the total SHG intensity as a function of the polarization angle of the excitation beam at $\lambda_{SHG} = 525$ nm for the flat and strained NbOI$_2$ regions. **c**, Temperature-dependent SHG at 298 K (red solid line) and 78 K (blue dashed line). **d**, Polarization versus electric field ($P-E$) hysteresis loop of NbOI$_2$ nanosheet at room temperature. **e**, SHG spectra as a function of the external electric field strength. An in-plane electric field is applied along the polar direction of the NbOI$_2$ nanosheet. The fundamental wavelength is 1,050 nm. The inset shows the peak SHG intensity as a function of external electric field strength.

highly efficient parametric conversion processes. Moreover, SHG can be used for the non-invasive visualization of nanoscale NbOI$_2$ ferroelectric domains that are otherwise challenging to probe (Supplementary Note 4). The white arrows in Supplementary Fig. 11 point out 180° domain walls separating oppositely polarized ferroelectric domains.

To probe the spatial dependence of the nonlinear response, the total SHG intensity (that is, without an analysing polarizer in the detection channel) is measured as a function of the input laser polarization. Figure 3d shows the SHG intensity maps of the NbOI$_2$ sample with excitation laser polarized along the non-polar direction. The results reveal that, outside the non-polar P_1–P_2 excitonic bands (consider the examples of $\lambda_{SHG} = 450$ nm in Fig. 3b,d and $\lambda_{SHG} = 750$ nm in Supplementary Fig. 12), d_{22} is the dominant coefficient of $\chi^{(2)}$ which leads to a dominant SHG signal for input light polarized in the polar direction as manifested in the anisotropic two-lobed SHG intensity pattern (Fig. 3e). The ratio of SHG intensities along the two in-plane axes exceeds 7 for $\lambda_{SHG} = 450$ nm; however, when the generated SHG signal is resonant with the energy of the P_1 and P_2 excitons (for example, $\lambda_{SHG} = 525$ nm), the strong resonance and localization effects greatly magnify the d_{16} coefficient, enhancing the SHG signal for input light polarized in the non-polar direction to be comparable with the polar signal and resulting in an isotropic, near-circular SHG intensity pattern. The SHG polar plots in Fig. 3e and the polar and non-polar SHG signals in Fig. 3f

clearly display this wavelength-dependent SHG anisotropy–isotropy cross-over. This contrasts with group-VI TMDs (for example, 2H-MoS$_2$), which show only isotropic SHG polar plots, and group-VII TMDs (for example, ReS$_2$), which show only anisotropic SHG polar plots for the total SHG intensity[40,41]. The polarization of the emitted SHG signal is also analysed and found to be strongly polarized along the non-polar direction, regardless of the excitation polarization (Supplementary Note 5 and Supplementary Fig. 13).

Manipulation of the nonlinear response. The structural polarity of NbOI$_2$ and, consequently, its nonlinear response, can be strongly modulated using external stimuli such as mechanical strain, temperature or an external electric field. Theoretically, the niobium polar displacement can be increased twofold by applying 3% tensile strain along the polar axis. The strong piezoelectric response predicted for NbOI$_2$ (ref. [19]) should lead to a strong built-in piezoelectric field and enhanced SHG signal in strained NbOI$_2$. To validate this, we introduced a localized uniaxial strain along the polar direction via the buckling-induced delamination process[42]. Figure 4a and Supplementary Fig. 14 depict buckling-induced NbOI$_2$ wrinkles separated by flat unstrained regions. The maximum tensile strain at the crest of the wrinkles is quantified by means of linear buckling theory and atomic force microscopy characterization (Supplementary Note 6 and Supplementary Fig. 15). The presence of both curved and flat areas in the same NbOI$_2$ flake allows their nonlinear optical

properties to be compared. We mapped the SHG intensity as a function of the spatial position of the sample with the pump polarized along the polar axis. As illustrated in Fig. 4a, in comparison to the flat areas, the $NbOI_2$ wrinkled regions (3.1% strain) show an up to 35-fold increase in the SHG intensity, reaching a record efficiency η_{SHG} of >0.2% ($\chi_{eff}^{(2)} \sim 113 \times 10^{-11}\,m\,V^{-1}$). Furthermore, the SHG polar plot of the strained area reveals that the isotropic SHG response (within the non-polar exciton band) vanishes due to the lengthening of the d_{22} coefficient (Fig. 4b). The high nonlinear conversion efficiency of $NbOI_2$ motivates multiple applications in classical and quantum photonics. For example, it can be utilized as an ultrathin pump for parametric downconverters to produce high-flux squeezed and entangled quantum states of light, with applications in quantum computation and quantum cryptography[43–45]. Aside from the strain engineering of the nonlinear response, the SHG intensity increases fivefold (Fig. 4c) upon reducing the temperature to 78 K, implying enhanced ferroelectric polarization. This is further confirmed by low-temperature SC-XRD measurements (Supplementary CIFs), showing that the niobium polar displacement extends from 0.14 Å at 298 K to 0.17 Å at 100 K.

The spontaneous polarization of a ferroelectric material, by definition, can be switched by an external electric field. The ferroelectric property of $NbOI_2$ is verified from its polarization versus electric field ($P–E$) characteristics (Fig. 4d) measured when an external electric field is applied along the polar direction. The curve exhibits a clear ferroelectric hysteresis loop (Supplementary Note 7). The coercive (E_c) and saturation (E_{sat}) fields are determined to be around $8.5\,kV\,cm^{-1}$ and $\pm17.5\,kV\,cm^{-1}$, respectively. We monitor the SHG intensity as a function of the applied in-plane electric field to study the dynamic properties of d_{22}-SHG, as shown in Fig. 4e for the positive electric field part. The SHG intensity increases rapidly once the coercive field threshold is overcome and eventually saturates, following the same trend as the polarization. The large modulation contrast (≥80%) of the SHG signal between two states (paraelectric at E_c and monodomain ferroelectric at E_{sat}) by the electric field can potentially enable electrically tunable integrated light sources (for example, frequency combs) for sensing and on-chip communication[46,47]. Similar dynamic control over the SHG signal is registered in the negative applied field region (Supplementary Fig. 16), affirming the polar switchability in $NbOI_2$ at room temperature. The polarization reversal (domain switching) in $NbOI_2$ implies that the sign of the nonlinear coefficient can be periodically reversed along the interaction length. This deterministic control of the sign and magnitude of the nonlinear coefficient at the nanoscale opens up a promising area for designing optical modulators and transistor devices with high SHG efficiencies for optical signal processing[48–50].

Conclusion. We demonstrate that polar two-dimensional $NbOI_2$ shows a very strong second-order parametric response. The strongly piezoelectric nature of $NbOI_2$ allows strain-tunable nonlinear response with a record SHG absolute conversion efficiency of >0.2% without purposefully considering phase-matching conditions. The spatial profile of the polarized SHG response can be modulated by resonance or off-resonance excitations, as well as strain. Taking advantage of the switchable ferroelectric polarization of $NbOI_2$, the SHG signal can be electrically modulated with modulation contrast exceeding 80%. Our work suggests that polar layered transition metal oxidehalides that combine strong piezoelectric and ferroelectric properties allow strain and polar order to be coupled with nonlinear responses, enabling a new generation of strain-tunable and electrical-tunable nonlinear optical devices.

Online content

Any methods, additional references, Nature Research reporting summaries, source data, extended data, supplementary information, acknowledgements, peer review information; details of author contributions and competing interests; and statements of data and code availability are available at https://doi.org/10.1038/s41566-022-01021-y.

References

1. Boyd, R. W. *Nonlinear Optics* 3rd edn (Academic, 2008).
2. Helk, T. et al. Table-top extreme ultraviolet second harmonic generation. *Sci. Adv.* **7**, eabe2265 (2021).
3. Shwartz, S. et al. X-ray second harmonic generation. *Phys. Rev. Lett.* **112**, 163901 (2014).
4. Trebino, R. et al. Measuring ultrashort laser pulses in the time-frequency domain using frequency-resolved optical gating. *Rev. Sci. Instrum.* **68**, 3277–3295 (1997).
5. Willner, A. E., Khaleghi, S., Chitgarha, M. R. & Yilmaz, O. F. All-optical signal processing. *J. Lightwave Technol.* **32**, 660–680 (2014).
6. Pantazis, P., Maloney, J., Wu, D. & Fraser, S. E. Second harmonic generating (SHG) nanoprobes for in vivo imaging. *Proc. Natl Acad. Sci. USA* **107**, 14535–14540 (2010).
7. Manaka, T., Lim, E., Tamura, R. & Iwamoto, M. Direct imaging of carrier motion in organic transistors by optical second-harmonic generation. *Nat. Photon.* **1**, 581–584 (2007).
8. Yin, X. et al. Edge nonlinear optics on a MoS₂ atomic monolayer. *Science* **344**, 488–490 (2014).
9. Shen, Y. Surface properties probed by second-harmonic and sum-frequency generation. *Nature* **337**, 519–525 (1989).
10. Hsieh, D. et al. Nonlinear optical probe of tunable surface electrons on a topological insulator. *Phys. Rev. Lett.* **106**, 057401 (2011).
11. Yakovlev, D. R. et al. Exciton spectroscopy of semiconductors by the method of optical harmonics generation (review). *Phys. Solid State* **60**, 1471–1486 (2018).
12. Chauleau, J.-Y., Haltz, E., Carrétéro, C., Fusil, S. & Viret, M. Multi-stimuli manipulation of antiferromagnetic domains assessed by second-harmonic imaging. *Nat. Mater.* **16**, 803–807 (2017).
13. Lin, K.-Q., Bange, S. & Lupton, J. M. Quantum interference in second-harmonic generation from monolayer WSe₂. *Nat. Phys.* **15**, 242–246 (2019).
14. Cui, C., Xue, F., Hu, W.-J. & Li, L.-J. Two-dimensional materials with piezoelectric and ferroelectric functionalities. *npj 2D Mater. Appl.* **2**, 1–14 (2018).
15. Schäber, H. & Gerken, R. Beiträge zur chemie der elemente niob und tantal. XXIX. NbOJ₃ und NbOJ₂. Darstellung, eigenschaften und thermisches verhalten. *Z. Anorg. Allg. Chem.* **317**, 105–112 (1962).
16. Rijnsdorp, J & Jellinek, F. The crystal structure of niobium oxide diiodide NbOI₂. *J. Less-Common Met.* **61**, 79–82 (1978).
17. Hillebrecht, H. et al. Structural and scanning microscopy studies of layered compounds MCl₃ (M = Mo, Ru, Cr) and MOCl₂ (M = V, Nb, Mo, Ru, Os). *J. Alloys Compd.* **246**, 70–79 (1997).
18. Beck, J. & Kusterer, C. Crystal structure of NbOBr₂. *Z. Anorg. Allg. Chem.* **632**, 2193–2194 (2006).
19. Wu, Y. et al. Data-driven discovery of high performance layered van der Waals piezoelectric NbOI₂. *Nat. Commun.* **13**, 1884 (2022).
20. Pugachev, A. et al. Broken local symmetry in paraelectric BaTiO₃ proved by second harmonic generation. *Phys. Rev. Lett.* **108**, 247601 (2012).
21. Clark, D. et al. Near bandgap second-order nonlinear optical characteristics of MoS₂ monolayer transferred on transparent substrates. *Appl. Phys. Lett.* **107**, 131113 (2015).
22. Woodward, R. et al. Characterization of the second-and third-order nonlinear optical susceptibilities of monolayer MoS₂ using multiphoton microscopy. *2D Mater.* **4**, 011006 (2016).
23. Säynätjoki, A. et al. Ultra-strong nonlinear optical processes and trigonal warping in MoS₂ layers. *Nat. Commun.* **8**, 1–8 (2017).
24. Seyler, K. L. et al. Electrical control of second-harmonic generation in a WSe₂ monolayer transistor. *Nat. Nanotechnol.* **10**, 407 (2015).
25. Karvonen, L. et al. Investigation of second- and third-harmonic generation in few-layer gallium selenide by multiphoton microscopy. *Sci Rep.* **5**, 10334 (2015).
26. Malard, L. M., Alencar, T. V., Barboza, A. P. M., Mak, K. F. & de Paula, A. M. Observation of intense second harmonic generation from MoS₂ atomic crystals. *Phys. Rev. B* **87**, 201401 (2013).
27. Wu, L. et al. Giant anisotropic nonlinear optical response in transition metal monopnictide Weyl semimetals. *Nat. Phys.* **13**, 350–355 (2017).
28. Bergfeld, S. & Daum, W. Second-harmonic generation in GaAs: experiment versus theoretical predictions of $\chi_{xyz}^{(2)}$. *Phys. Rev. Lett.* **90**, 036801 (2003).
29. Shoji, I., Kondo, T., Kitamoto, A., Shirane, M. & Ito, R. Absolute scale of second-order nonlinear-optical coefficients. *JOSA B* **14**, 2268–2294 (1997).

30. Yariv A. & Yeh P. *Photonics: Optical Electronics in Modern Communications* (Oxford Univ. Press, 2007).
31. Shen, Y. R. *The Principles of Nonlinear Optics* (Wiley. 1984).
32. Peierls R. E. *Quantum Theory of Solids* (Clarendon, 1996).
33. Jia, Y., Zhao, M., Gou, G., Zeng, X. C. & Li, J. Niobium oxide dihalides $NbOX_2$: a new family of two-dimensional van der Waals layered materials with intrinsic ferroelectricity and antiferroelectricity. *Nanoscale Horiz.* **4**, 1113–1123 (2019).
34. Hybertsen, M. S. & Louie, S. G. Electron correlation in semiconductors and insulators: band gaps and quasiparticle energies. *Phys. Rev. B* **34**, 5390–5413 (1986).
35. Hedin, L. New method for calculating the one-particle Green's function with application to the electron-gas problem. *Phys. Rev.* **139**, A796–A823 (1965).
36. Rouxel J. *Crystal Chemistry and Properties of Materials with Quasi-One-Dimensional Structures: A Chemical and Physical Synthetic Approach* (D. Reidel, 1986).
37. Fang, Y., Wang, F., Wang, R., Zhai, T. & Huang, F. 2D $NbOI_2$: a chiral semiconductor with highly in-plane anisotropic electrical and optical properties. *Adv. Mater.* **33**, 2101505 (2021).
38. Bloembergen, N. & Pershan, P. S. Light waves at the boundary of nonlinear media. *Phys. Rev.* **128**, 606–622 (1962).
39. Hopfield, J. J. & Thomas, D. G. Theoretical and experimental effects of spatial dispersion on the optical properties of crystals. *Phys. Rev.* **132**, 563–572 (1963).
40. Li, Y. et al. Probing symmetry properties of few-layer MoS_2 and h-BN by optical second-harmonic generation. *Nano Lett.* **13**, 3329 (2013).
41. Song, Y. et al. Extraordinary second harmonic generation in ReS_2 atomic crystals. *ACS Photon.* **5**, 3485–3491 (2018).
42. Vella, D., Bico, J., Boudaoud, A., Roman, B. & Reis, P. M. The macroscopic delamination of thin films from elastic substrates. *Proc. Natl Acad. Sci. USA* **106**, 10901–10906 (2009).
43. Fickler, R. et al. Quantum entanglement of high angular momenta. *Science* **338**, 640–643 (2012).
44. Fedrizzi, A., Herbst, T., Poppe, A., Jennewein, T. & Zeilinger, A. A wavelength-tunable fiber-coupled source of narrowband entangled photons. *Opt. Express* **15**, 15377–15386 (2007).
45. Zhang, G. et al. An integrated silicon photonic chip platform for continuous-variable quantum key distribution. *Nat. Photon.* **13**, 839–842 (2019).
46. Hickstein, D. D. et al. Self-organized nonlinear gratings for ultrafast nanophotonics. *Nat. Photon.* **13**, 494–499 (2019).
47. Tran, R. J., Sly, K. L. & Conboy, J. C. Applications of surface second harmonic generation in biological sensing. *Ann. Rev. Anal. Chem.* **10**, 387–414 (2017).
48. Miller, D. A. B. Are optical transistors the logical next step? *Nat. Photon.* **4**, 3–5 (2010).
49. Gallo, K. & Assanto, G. All-optical diode based on second-harmonic generation in an asymmetric waveguide. *JOSA B* **16**, 267–269 (1999).
50. Fejer, M. M., Magel, G. A., Jundt, D. H. & Byer, R. L. Quasi-phase-matched second harmonic generation: tuning and tolerances. *IEEE J. Quantum Electron.* **28**, 2631–2654 (1992).

Methods

Crystal growth. $NbOI_2$ single crystals were grown by chemical vapour transport. $NbOI_2$ crystals were synthesized from high-purity niobium (film), iodine (crystals) and Nb_2O_5 (powder), which were mixed to form a stoichiometric ratio of Nb:O:I = 1:1:2, which was then sealed in the evacuated (10^{-5} mbar) quartz ampule. Sealed ampules were placed in the horizontal dual-zone furnace and brought to 600 °C at a rate of 1 °C per min. The ampules were held at 600 °C for five days and then slowly cooled for ten days with the slightly different rates at the hot (1.2 °C per hour) and cold (1.5 °C per hour) zones. This small temperature gradient ensured the growth of centimetre-size high-quality crystals near the cold end of the ampule. After the slow-cooling process, the furnace was turned off allowing the ampules to cool down naturally. Crystals were extracted from the opened ampules under inert conditions of an N_2-filled glove box and then stored for future use.

X-ray crystallographic analysis. The SC-XRD data were collected at room ($T = 298$ K) and low ($T = 100$ K) temperatures on a Bruker D8 Venture SC-XRD system equipped with molybdenum Kα radiation ($\lambda = 0.71073$ Å), a KAPPA four-circle goniometer, a PHOTON 100 detector (CMOS APS) and an Oxford Cryostream. Data collection, integration and scaling were carried out using the Bruker APEX3 software package[51]. The frames were integrated with the Bruker SAINT software package using a narrow-frame algorithm. Data were corrected for absorption effects using the multi-scan method (SADABS). The structures were solved and refined using the Bruker SHELXTL software package[52], using the space group C121, with $Z = 4$ for the formula unit, I_2NbO. The final anisotropic full-matrix least-squares refinement was performed on weighted F^2 values. Relevant crystal, collection and refinement data for the crystal structures of $NbOI_2$ at 298 K and 100 K are summarized in Supplementary Table 1. The crystallographic axes of the $NbOI_2$ crystals were identified from the SC-XRD analysis.

ARPES measurement. High-resolution ARPES measurements were performed in an ultrahigh-vacuum system under a pressure lower than 8×10^{-10} mbar. The ARPES chamber is equipped with a differentially pumped UVS300 helium discharge lamp (SPECS GmbH) as the light source, which provides monochromatized photon energies of 21.2 eV (He-I) and 40.8 eV (He-II) through a toroidal mirror monochromator (SPECS GmbH). Here we used He-I as the ARPES source. The temperature of the $NbOI_2$ bulk sample was kept at 77 K during the measurement.

Spectroscopic ellipsometry. The anisotropic in-plane complex refractive indices of $NbOI_2$ were characterized through Mueller matrix spectroscopic ellipsometry measurements; spectra within the spectral range 6.2–0.65 eV (200–1,900 nm), in steps of 20 meV, were obtained using a commercial rotating analyser instrument with a compensator (VASE, J.A. Woollam Co.). The samples were mounted on a precision rotation stage (RS40, Newport) to perform azimuth-dependent measurements, and the in-plane rotation angle ϕ was varied from 0° to 360°. At each in-plane orientation, data were taken at three angles of incidence a (50°, 60°, 70°). Such an angle-resolved measurement scheme is necessary for accessing the entire Mueller matrix and characterizing optically anisotropic samples[53–57].

Thin sample preparation. For linear absorption and SHG characterizations, the bulk $NbOI_2$ crystals were mechanically exfoliated onto clean quartz substrates using the Scotch tape method. Atomic force microscopy was used to measure the thickness of the exfoliated flakes. The flakes were covered with a thin layer of hexagonal boron nitride (h-BN, < 10 nm) using the poly(dimethyl siloxane) stamp-transfer method to avoid any photo-oxidation effects during the SHG measurements. For the field-dependent SHG measurements, $NbOI_2$ devices were prepared by transferring thin $NbOI_2$ flakes onto laterally interdigitated electrodes via poly(dimethyl siloxane) stamping. The electrodes (Pt (70 nm)/Ti (30 nm)) were patterned on SiO_2/Si wafers ($SiO_2 = 300$ nm) using electron beam lithography, electron beam evaporation and a lift-off process. A transfer station with an optical microscope and a rotating stage was used to transfer the $NbOI_2$ flakes in such a way that the device's lateral electrical field is aligned with the in-plane polar axis of the transferred flakes.

Optical, electrical and optoelectronic characterizations. The micro-absorption measurement was performed by placing the $NbOI_2$ sample between aligned microscope objectives (50X Mitutoyo, apochromat, infinity corrected), for light focusing and collection. Pulsed laser (Coherent Libra) with a fundamental wavelength of 800 nm, pulse width of ~50 fs, and repetition rate of 1 kHz, was focused on a sapphire crystal to generate a broadband white light. The light was passed through a 750 nm short-pass filter to eliminate the residual from the fundamental, before collimation using a parabolic mirror. The light was then sent to the objective and focused into ~2 μm spot for the absorption measurement. The absorption spectra were obtained by comparing the transmitted light spectra between the samples and a blank (quartz). Spectral detection was performed using a monochromator (Princeton Instrument) and a photomultiplier tube set-up. We used a femtosecond-pulsed Yb:KGW PHAROS laser system pumping

of a collinear optical parametric amplifier, ORPHEUS, with a LYRA wavelength extension (Light Conversion Ltd, pulse duration of 180 fs, repetition rate of 200 kHz, tunable output of 210 nm to 2,200 nm) for the SHG measurements. The excitation beam was focused onto the sample with a ×100 (NA = 0.9) air objective from Nikon (~1 μm² spot size). The spectral range of the excitation beam was tuned from 700 to 1,500 nm in steps of 50 nm. The nonlinear emission was collected in a back-scattering configuration via the same objective, and detected with an avalanche photodiode (MPD PDM Series by PicoQuant) for imaging, or by a spectrograph (PI Acton SP2300 by Princeton Instruments) for spectral measurements. The sample was fixed to an XYZ piezo-scanner stage (Nano-Drive, Mad City Labs) to perform the sample scanning. The excitation and detection polarizations were controlled with half- or quarter-wave plates, in combination with linear polarizers. The power of the collected SHG emission was measured with a calibrated silicon photodetector (Newport), whereas the excitation power was characterized with a germanium photodetector (Thorlabs). A continuous-flow optical microscopy cryostat was used for the low-temperature measurements. For the electric-field switchable SHG measurements, the SHG signal was recorded while the drain−source bias (supplied by Keithley Model 6430 Sub-Femtoamp Remote SourceMeter) was swept forward and backward. The polarization−electric field (P−E) curve was recorded using a ferroelectric tester (Precision Multiferroic II, Radiant Technologies).

Computational methods. The ab initio DFT calculations are performed using Quantum ESPRESSO[58,59] working with Perdew–Becke–Ernzerhof-optimized norm-conserving Vanderbilt pseudopotentials[60,61]. The full relaxations of the $NbOI_2$ atomic structures are performed with Semiempirical Grimme's D3 correction[62] using the conjugate gradient scheme until the maximum residual force smaller than 1×10^{-7} a.u. and the maximum energy difference between consecutive iterations is smaller than 1×10^{-9} Ry. A kinetic energy cut-off of 80 Ry for the pseudopotential and a Monkhorst-pack k-point mesh[63] of $12 \times 6 \times 1$ is used. A vacuum height of 12 Å is added to prevent interactions between the periodic images. The GW calculation is performed with BerkeleyGW[34,64,65] on top of Quantum ESPRESSO with slab coulomb truncation[66], Hybertsen-Louie generalized plasmon pole model[34] and a dielectric matrix cut-off of 10 Ry. The non-uniform neck subsampling is used to sample the reciprocal space in GW[67]. The GW quasiparticle energies are calculated with 1,536 bands, using a $12 \times 6 \times 1$ q-mesh with another 10 q-points in the Voronoi cell around $q = 0$, forming an effective uniform grid of more than $120 \times 60 \times 1$.

Data availability

The data supporting the findings of this study are available within the article and its Supplementary Information, or from the corresponding authors on reasonable request. The X-ray crystallographic coordinates for structures reported in this study have been deposited at the Cambridge Crystallographic Data Centre (CCDC), under deposition nos. 2169918-2169919. These data can be obtained free of charge from the Cambridge Crystallographic Data Centre via www.ccdc.cam.ac.uk/data_request/cif.

References

51. Bruker APEX3 (Bruker Nano, Inc., 2019).
52. Sheldrick, G. M. SHELXT–Integrated space-group and crystal-structure determination. *Acta Crystallogr. A Found. Adv.* **71**, 3–8 (2015).
53. Schubert M. *Infrared Ellipsometry on Semiconductor Layer Structures: Phonons, Plasmons, and Polaritons* Vol. 209 (Springer, 2004).
54. Losurdo M. & Hingerl K. *Ellipsometry at the Nanoscale* (Springer, 2013).
55. Schmidt, D. et al. Monoclinic optical constants, birefringence, and dichroism of slanted titanium nanocolumns determined by generalized ellipsometry. *Appl. Phys. Lett.* **94**, 011914 (2009).
56. Schmidt, D. et al. Generalized ellipsometry for monoclinic absorbing materials: determination of optical constants of Cr columnar thin films. *Opt. Lett.* **34**, 992–994 (2009).
57. Schubert, M. Polarization-dependent optical parameters of arbitrarily anisotropic homogeneous layered systems. *Phys. Rev. B* **53**, 4265–4274 (1996).
58. Giannozzi, P. et al. QUANTUM ESPRESSO: a modular and open-source software project for quantum simulations of materials. *J. Phys. Condens. Matter* **21**, 395502 (2009).
59. Giannozzi, P. et al. Advanced capabilities for materials modelling with Quantum ESPRESSO. *J. Phys. Condens. Matter* **29**, 465901 (2017).
60. Hamann, D. R. Optimized norm-conserving Vanderbilt pseudopotentials. *Phys. Rev. B* **88**, 085117 (2013).
61. Perdew, J. P., Burke, K. & Ernzerhof, M. Generalized gradient approximation made simple. *Phys. Rev. Lett.* **77**, 3865–3868 (1996).
62. Grimme, S. Semiempirical GGA-type density functional constructed with a long-range dispersion correction. *J. Comput. Chem.* **27**, 1787–1799 (2006).
63. Monkhorst, H. J. & Pack, J. D. Special points for Brillouin-zone integrations. *Phys. Rev. B* **13**, 5188–5192 (1976).
64. Rohlfing, M. & Louie, S. G. Electron-hole excitations and optical spectra from first principles. *Phys. Rev.B* **62**, 4927–4944 (2000).

65. Deslippe, J. et al. BerkeleyGW: a massively parallel computer package for the calculation of the quasiparticle and optical properties of materials and nanostructures. *Comput. Phys. Commun.* **183**, 1269–1289 (2012).

66. Ismail-Beigi, S. Truncation of periodic image interactions for confined systems. *Phys. Rev. B* **73**, 233103 (2006).

67. da Jornada, F. H., Qiu, D. Y. & Louie, S. G. Nonuniform sampling schemes of the Brillouin zone for many-electron perturbation-theory calculations in reduced dimensionality. *Phys. Rev. B* **95**, 035109 (2017).

Author contributions

I.A., S.A.M. and K.P.L. conceived the project and designed the experiments. I.A. performed micromechanical cleavage, two-dimensional dry transfer, device fabrication and material characterization under the supervision of S.A.M. and K.P.L. I.A., B.T., D.G. and R.B. performed all the optical characterizations under the guidance of L.d.S.M., T.C.S., S.A.M., and K.P.L. Y.W. and F.X. performed the calculations and theoretical analysis under supervision of S.Y.Q. I.V. synthesized the $NbOI_2$ bulk crystals under the supervision of G.E. M.Z. performed the ARPES measurements. I.A. wrote the manuscript with input from all authors.

Competing interests

The authors declare no competing interests.

Additional information

Supplementary information The online version contains supplementary material available at https://doi.org/10.1038/s41566-022-01021-y.

Correspondence and requests for materials should be addressed to Stefan A. Maier or Kian Ping Loh.

Peer review information *Nature Photonics* thanks Mikhail Glazov and the other, anonymous, reviewer(s) for their contribution to the peer review of this work.

Reprints and permissions information is available at www.nature.com/reprints.